Highlights

Exploring Impact Vapor Plume Reactions from Asteroidal Impacts: Monte Carlo Simulations and Implications for Biomolecules Synthesis

Yoko Ochiai,Shigeru Ida,Daigo Shoji

- A Monte Carlo simulation we developed was applied to chemical reactions in impact vapor plumes

- Compositional evolution of vapor plumes was calculated for three different impactor materials

- The simulations demonstrated the synthesis of diverse organic molecules without predefined reaction pathways

- Key precursors to biomolecules were identified among the synthesized organic molecules

- Results suggest biomolecules are formed through liquid-phase reactions after H_2O condenses during plume cooling

Exploring Impact Vapor Plume Reactions from Asteroidal Impacts: Monte Carlo Simulations and Implications for Biomolecules Synthesis

Yoko Ochiai[a], Shigeru Ida[a] and Daigo Shoji[b]

[a]Earth-Life Science Institute, Institute of Science Tokyo, 2-12-1 Ookayama, Meguro-ku, Tokyo, 152-8550, Japan
[b]Institute of Space and Astronautical Science, Japan Aerospace Exploration Agency, 3-1-1 Yoshinodai, Chuo-ku, Sagamihara, Kanagawa, 252-5210, Japan

ARTICLE INFO

ABSTRACT

During a hypervelocity impact, both the impactor and target materials evaporate, generating an impact vapor plume with temperatures reaching several thousand K. As the plume cools through adiabatic expansion, chemical reactions are predicted to quench, leading to a non-equilibrium composition. Previous experiments simulating meteorite impacts on the early Earth have reported the formation of biomolecules such as amino acids and nucleobases, suggesting that the chemical reactions within impact vapor plumes may have contributed to the origins of the building blocks of life. However, it is still unclear how chemical reactions proceed during the cooling impact vapor plume and lead to the synthesis of such organic molecules. In this study, to investigate the evolution of chemical composition within impact vapor plumes, we conducted a Monte Carlo chemical reaction simulation for complex organic synthesis, developed in our previous work (Ochiai, Y., Ida, S., Shoji, D., [2024], Astron. Astrophys., 687, A232). In conventional kinetic model-based studies, chemical species and their associated reaction pathways are predefined to calculate the time evolution of chemical compositions using the thermodynamic data of these species and reaction rate coefficients. In contrast, our model does not rely on a predefined reaction network; instead, it utilizes imposed conditions for chemical changes and an approximate method for calculating reaction rates suited to our objectives. Additionally, we developed a new approach to couple these chemical reaction calculations with the rapid temperature and pressure decay in the vapor plume. Results show diverse organic molecule production depending on the impactor materials assumed in this study (LL, CI, and EL chondritic types). These products include important precursors to biomolecules such as amino acids, sugars, and nucleobases. On the other hand, for all impactor compositions, the abundance of biomolecules themselves remains extremely low throughout the reactions from an impact to quenching. Therefore, our results suggest that biomolecules are not directly produced in impact vapor plumes but rather synthesized through reactions of these precursor molecules in aqueous solutions, following H_2O condensation as the vapor plume cools. Many of the detected organic compounds, including the precursor molecules such as imine compounds and formamide, are not included in the reaction networks of previous kinetic model simulations, and their formation has not been predicted. This demonstrates the effectiveness of our Monte Carlo simulation as a powerful tool for investigating the synthesis of low-abundance organic compounds, including biomolecules.

1. Introduction

The origin of the building blocks of life remains a critical question in understanding the emergence of life. Organic synthesis triggered by meteorite impacts has been discussed as a potential mechanism for providing biomolecules to the early Earth (e.g., Bar-Nun et al., 1970; McKay and Borucki, 1997). During hypervelocity impacts, the impactor materials are vaporized, forming a vapor plume rich in volatile elements such as carbon (C), nitrogen (N), oxygen (O), and hydrogen (H) (e.g., Sugita and Schultz, 2003a,b). Due to the extremely high temperature and pressure within a vapor plume, chemical reactions can proceed vigorously, potentially leading to the synthesis of organic molecules (e.g., Mukhin et al., 1989). Previous studies have reported the formation of biomolecules, including amino acids and nucleobases, in shock-recovery experiments (Furukawa et al., 2008, 2015; Takeuchi et al., 2020) and in laser shock wave plasma experiments (Ferus et al., 2017) simulating meteorite impacts on the early Earth.

✉ ochiai@elsi.jp (Y. Ochiai); ida@elsi.jp (S. Ida); shohji.daigo@jaxa.jp (D. Shoji)
ORCID(s): 0009-0007-9894-3590 (Y. Ochiai)

Consequently, impact events in the early Earth, particularly during the Late Heavy Bombardment (LHB) when the frequency of impacts was significantly high after the ocean was formed (e.g., Bottke and Norman, 2017; Lowe and Byerly, 2018, and references therein), may have played a crucial role in the emergence of life. However, the current understanding of chemical reactions within an impact vapor plume is limited, and the specific reaction pathways leading to the synthesis of complex biomolecules, as observed in experimental studies, remain unclear. Therefore, this study aims to elucidate the mechanisms of organic synthesis within impact vapor plumes, focusing on amino acids, one of the biomolecules identified in impact experiments.
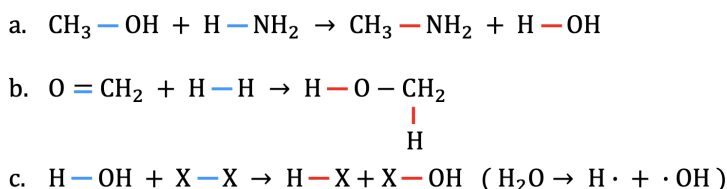
The post-shock temperature of vapor plumes can reach extremely high values (>1000 K) as part of the impact energy is converted into the thermal energy (e.g., Pierazzo et al., 1998). Following the impact, the vapor plume undergoes adiabatic expansion and rapid cooling on a timescale of a few seconds. Initially, the vapor plume attains thermodynamic equilibrium, as chemical reactions occur rapidly compared to the cooling rate. However, since reaction rates highly depends on the temperature, the timescale for chemical reactions increases significantly as the vapor cools. Consequently, chemical reactions within the vapor plume are quenched during the cooling. Although quench temperatures depend on impact conditions and molecular species, they are generally predicted to fall within the range of $1000 - 3000$ K (e.g., Gerasimov et al., 1999; Fegley et al., 1986; Ishimaru et al., 2010).

Ishimaru et al. (2010) investigated the quenching process of chemical reactions within a vapor plume using a chemical kinetic model, which calculates the temporal evolution of chemical species concentrations based on the reaction rates of elementary reactions. To account for both chemical reactions and the changes in temperature and pressure within the vapor plume, they coupled the chemical kinetic model with a one-dimensional radial hydrodynamic calculation, in which the expanding vapor plume was approximated as a gas hemisphere. Their results demonstrated that not only the quenching temperatures vary between species, but the quenched abundances can also deviate–by a factor of 5 to 9 in the case of HCN–from those estimated by the equilibrium compositions of the temperature at which the timescale of decomposition of that species is equal to the cooling timescale. This suggests that the quenched composition cannot be simply inferred from equilibrium composition, and that the chemical reactions within the vapor plume should be addressed using a kinetic approach. However, kinetic models require the prior specification of all the reactions included in the model, which can introduce biases into the reaction networks (set of chemical species and their associated elementary reactions). The kinetic model (GRI-Mech version 3.0) used by Ishimaru et al. (2010) was originally developed to simulate combustion reactions of small hydrocarbons, such as methane and ethane, and may not account for potential products, including complex organic compounds, in impact vapor plumes. Therefore, to avoid excluding important potential reactions, an alternative approach that does not assume specific reaction pathways is needed.

Ab initio molecular dynamics (AIMD) simulations provide a method for simulating chemical reactions without the need for predefined reaction pathways and parameters, relying solely on quantum mechanical principles. Goldman et al. (2010), Goldman and Tamblyn (2013) and Shimamura et al. (2019) employed AIMD simulations to investigate post-shock reactions following the impacts of a comet and an Fe-bearing meteorite, respectively, with a focus on the synthesis of organic molecules. Goldman et al. (2010) demonstrated the formation of C-N bonded oligomers following compression, suggesting that complex organic molecules could be synthesized within vapor plumes. However, the timescale applicable to chemical reactions in AIMD simulations is generally constrained to a few picoseconds due to the high computational costs involved. This limitation presents a challenge for achieving a comprehensive understanding of the quenching process, which occurs over a timescale of several seconds.

Therefore, in this study, we employed the Monte Carlo simulation method for chemical reactions developed in our previous works (Takehara et al., 2022; Ochiai et al., 2024). In this method, a set of molecules is specified, and all possible reactions among them are listed. A single reaction is then selected based on probabilities weighted by reaction rates, and the molecular set is updated accordingly. By iterating this selection process, we perform a Monte Carlo simulation of chemical reactions that incorporates chemical kinetics without the need for predefined reaction networks. This model significantly reduces computational costs by evaluating the reaction rates approximately, allowing for the exploration of the complete reaction process in a vapor plume until quenching occurs. The adopted approximations are appropriate for our purpose, which is to obtain a comprehensive overview of chemical reactions leading to complex organic molecules. Due to this approximation, some degree of inaccuracy in the reaction rates is inevitable, making this method less suitable for determining the precise concentrations of individual chemical species in the system. However, because this model considers all potential reaction pathways with relatively low computational cost, it is well-suited for exploring the synthesis of organic molecules involving complex reaction pathways that are difficult to capture with conventional kinetic models. Notably, our simulation results showed the synthesis of key precursors to biomolecules in

Examples of chemical reactions in this model

    a. $\mathrm{CH_3 - OH} + \mathrm{H - NH_2} \rightarrow \mathrm{CH_3 - NH_2} + \mathrm{H - OH}$

    b. $\mathrm{O = CH_2} + \mathrm{H - H} \rightarrow \mathrm{H - O - CH_2}$
$$\qquad\qquad\qquad\qquad\qquad\qquad\quad |$$
$$\qquad\qquad\qquad\qquad\qquad\qquad\quad \mathrm{H}$$

    c. $\mathrm{H - OH} + \mathrm{X - X} \rightarrow \mathrm{H - X} + \mathrm{X - OH} \quad (\mathrm{H_2O} \rightarrow \mathrm{H \cdot} + \cdot\mathrm{OH})$

Figure 1: Examples of chemical reactions considered in this model. In each reaction, bonds being broken are colored blue, and bonds being formed are colored red. As shown in the second reaction, double bonds (and triple bonds) are treated as two (or three) independent bonds. The atom X shown in the third reaction is a hypothetical element used to represent radical species within our reaction scheme (see Section 2.1).

the impact vapor plume, which were not included in the reaction network model used by the previous study (Ishimaru et al., 2010), as shown in Section 3.2.

The original model in Ochiai et al. (2024) was primarily developed to simulate surface reactions of icy dust particles driven by UV irradiation in protoplanetary disk environments ($\sim 50 - 100$ K). Hence, several modifications were made to adapt the model for our current study. First, we introduced the consideration of entropy changes in reactions to accommodate gas-phase reactions, which occur at higher temperatures than ice surface reactions. Additionally, we developed a method to couple the Monte Carlo simulations with temporal changes in temperature and pressure, enabling the model to simultaneously track the chemical reactions and the rapid temperature and pressure change occurring within the vapor plume over time. Details of these updates are provided in Section 2.2.

In Section 2, we describe the fundamental methodology of the Monte Carlo simulation developed by Ochiai et al. (2024), along with the updates applied in this study. We also explain the procedures for calculating temperature and pressure variations within an impact vapor plume and how these calculations are integrated with the chemical reaction simulations. Additionally, we detail the initial conditions for the simulations, including the initial temperature, pressure, and composition of the impact vapor plumes. In Section 3, we present the compositional evolution of vapor plumes for three different impactor materials, focusing on the mole fraction changes of major chemical species and organic molecules. Our results show the synthesis of a wide variety of organic molecules within impact vapor plumes, including species not accounted for in the reaction network used in previous study. Furthermore, some of these organic products may play crucial roles in subsequent biomolecule synthesis. In Section 4, we discuss the potential influence of the approximations used in estimating reaction rates and the omission of rock-forming elements in impact vapor plumes in this study. In Section 5, we summarize our results.

2. Method

In this section, we briefly explain a numerical method of the Monte Carlo simulation proposed in Ochiai et al. (2024) and the modifications newly made in this study to account for asteroid impacts. The basic scheme of the Monte Carlo simulation presented in Section 2.1 follows directly the one employed in Ochiai et al. (2024). However, the underlying environmental conditions represented by temperature T and pressure P differ from the previous model (see Section 2.3 and Section 2.4). Thus, the weight of probabilities to choose a next reaction from the reaction candidates, explained in Section 2.2, was updated to a more general version than that in Ochiai et al. (2024) to apply the simulation for higher-temperature environments such as asteroid impacts, as well as the low temperature environments such as icy dust surface exposed to UV irradiation. We emphasize that the strength of our simulation model lies in its versatility: it can be applied to the synthesis of organic molecules in diverse environments and under different physical and chemical processes, simply by adjusting the environmental conditions while maintaining the same fundamental scheme.

2.1. Basic Scheme of the Monte Carlo Simulation: Tracking Chemical Reaction Sequences

The fundamental unit of this Monte Carlo simulation is a molecular set consisting of several dozen molecules and/or radicals. Every chemical species within a molecular set are characterized by its constituent atoms and the bonds between these atoms. The initial step in a chemical reaction simulation is to list the all chemical reaction candidates

Bond energy [kJ/mol]					
C − C	347	N − N	161	O − O	146
C = C	611	N = N	456	O = O	498
C ≡ C	837	N ≡ N	946		
C − N	305	C − O	358	N − O	230
C = N	615	C = O	745*	N = O	598
C ≡ N	891	C ≡ O	1072		
C − H	414	N − H	389	O − H	464
H − H	436				

Table 1
Bond energies used in this study (Sanderson, 1976). (*) For CO_2, the C=O double bond energy is 799 kJ/mol instead of 745 kJ/mol.

that are possible to occur within the molecular set. However, the reactions listed here are limited to the exchange of two bonds, specifically the breaking and recombination of two bonds, which represent the minimal components of chemical reactions. Examples of chemical reactions considered in this simulation are shown in Fig. 1. Next, a single reaction is randomly selected from the candidates based on the weighted probabilities evaluated from reaction rates (see Section 2.2). Then, the molecular set after the selected chemical reaction occurs is designated as a new starting set. We refer to this entire series of calculations up to this point as a single reaction step.

For a given initial condition, the reaction calculation up to a specific reaction step number is performed multiple times (typically 10^3 trials in this study) using different random number seeds to ensure sufficient sampling. Consequently, the statistical molecular evolution in the molecular set is obtained.

To represent radical reactions, we use a hypothetical molecule, X_2, following Ochiai et al. (2024). X_2 is not a physically existing molecule, but an element used solely for computational purposes. Using a water molecule as an example, a radical formation reaction can be written as Fig. 1c. The products, H-X and X-OH, represent an H radical and an OH radical, respectively. The bond to an X atom indicates the presence of an unpaired electron on the binding atom, and its bond energy is therefore set to be zero. By introducing X_2, radical reactions, which do not physically involve the exchange of two bonds, are still formally treated as chemical reactions within this model, defined as the exchange of two bonds. In Ochiai et al. (2024), the X-X bond energy was assigned a negative value to represent the photon energy associated with UV irradiation in a protoplanetary disk. Since photon irradiation is not considered in this study, the bond energy of X_2 is set to zero.

2.2. Probability weighting and estimation of reaction rates

In this section, we explain how the probabilities for the reaction candidates are weighted during the chemical reaction calculations described earlier. In this study, we adopted a different form of the weight from the one used in the previous model by Ochiai et al. (2024).

In Ochiai et al. (2024), the probability weighting for each reaction, W, was given as follows:

$$W = \exp\left(-\frac{E_\mathrm{a}}{RT}\right), \tag{1}$$

where E_a is the activation energy of the reaction. This activation energy in Eq. (1) was evaluated using the Bell–Evans–Polanyi principle:

$$E_\mathrm{a} = \alpha' \Delta H + \beta', \tag{2}$$

where ΔH is the enthalpy change of the reaction, and α' and β' are empirical parameters. According to density functional theory (DFT) calculations (Michaelides et al., 2003; Wang et al., 2011; Sutton and Vlachos, 2012), $\alpha' = 1$ and $\beta' = 100$ kJ/mol were adopted for fiducial values in Ochiai et al. (2024). The enthalpy change ΔH was approximately calculated in the same manner as this study (see below). This Arrhenius-type weight reflected the relative magnitude of the reaction rates among the candidate reactions, but it did not explicitly account for reaction timescales and differences between first- and second-order reactions. Furthermore, since Ochiai et al. (2024) focused on systems where non-equilibrium states are maintained through reactions, consistency with thermodynamic equilibrium was not considered, which is important for high-temperature chemistry in an impact vapor plume.

Thus, in this study, while following the framework that incorporates individual reaction rates into the simulation by weighting the probability of each reaction, we apply a modified weighting formula adjusted to the conditions of the impact vapor plume. As explained in Section 2.3, we incorporate the time evolution of temperature and pressure within the vapor plume into chemical reaction calculations. To achieve this, the timescales of chemical reactions are required, necessitating the estimation of the absolute values of reaction rates. Therefore, in this study, we employ the Eyring equation to derive the reaction rates and directly use them to weight the probabilities instead of the previous weight equation (1). The Eyring equation is based on the the transition state theory, which assumes the quasi-equilibrium between reactants and activated transition state complexes, and is written as follows:

$$k_{\text{first}} = \frac{\kappa k_{\text{B}} T}{h} \exp\left(-\frac{\Delta^{\ddagger} G^{\circ}}{RT}\right),$$ (3)

$$k_{\text{second}} = \frac{\kappa k_{\text{B}} T}{h} \left(\frac{RT}{P^{\circ}}\right) \exp\left(-\frac{\Delta^{\ddagger} G^{\circ}}{RT}\right),$$ (4)

where k_{first} and k_{second} are the rate constants of first-order reactions and second order reactions, respectively, κ is the transmission coefficient, k_{B} is the Boltzmann constant, R is the gas constant, T is the temperature, h is the Planck constant, P° is the standard pressure (1 bar), and $\Delta^{\ddagger} G^{\circ}$ is the standard Gibbs energy of activation (the difference in Gibbs energies between reactants and activated transition state complexes in their standard states). We assume that the $\kappa = 1$ in this study.

To calculate $\Delta^{\ddagger} G^{\circ}$, we assume the linear relationship between the standard Gibbs energy of activation $\Delta^{\ddagger} G^{\circ}$ and the standard reaction Gibbs energy $\Delta_r G^{\circ}$ (the difference in Gibbs energies between reactants and products in their standard states), as follows:

$$\Delta^{\ddagger} G^{\circ} = \alpha \Delta_r G^{\circ} + \beta,$$ (5)

where α and β are the constants specified by the reaction type. Although such linear relationships have been identified in many reactions in previous studies using quantum chemical calculations (e.g., Salamone et al., 2021; Yang and Saidi, 2024), how α and β are determined for a given reaction has not yet been formulated. Thus, in this study, we assume $\alpha = 0.5$ and β in the range of $250 - 350$ kJ/mol, with $\beta = 300$ kJ/mol as the fiducial value, based on comparisons between our calculations and the results of Ishimaru et al. (2010) (see Appendix A for a detailed explanation of assumptions α and β).

The standard reaction Gibbs energy $\Delta_r G^{\circ}$ is expressed in terms of the standard reaction enthalpy $\Delta_r H^{\circ}$, temperature T, and the standard reaction entropy $\Delta_r S^{\circ}$, as follows:

$$\Delta_r G^{\circ} = \Delta_r H^{\circ} - T \Delta_r S^{\circ}.$$ (6)

Since $\Delta_r H^{\circ} \sim O(100)$ kJ/mol and $\Delta_r S^{\circ} \sim O(0.1)$ kJ/mol (see Tables 1 and 2), the entropy term is negligible for $T \sim 50 - 100$ K, as considered by Ochiai et al. (2024). However, because the temperature in an impact vapor plume generated by an asteroid impact can exceed 1000 K, accounting for entropy changes becomes essential. Therefore, in this study, $\Delta_r H^{\circ}$ and $\Delta_r S^{\circ}$ are calculated using the methods described below.

As in the previous model, $\Delta_r H^{\circ}$ is given by the difference in the total bond energies (sum of the bond energies of the individual bonds that constitute a molecule) of reactants and products of each reaction. Bond energies used in this study are shown in Table 1.

For the calculation of $\Delta_r S^{\circ}$, we approximate entropy by considering only the contribution from translational motion, as follows (Atkins et al., 2017):

$$\begin{aligned}
\frac{S_{\text{m}}}{R} &\simeq \frac{2}{3} + \frac{3}{2} \ln\left(\frac{2\pi M k_{\text{B}} T}{h^2}\right) - \ln\left(\frac{P}{k_{\text{B}} T}\right) + 1 \\
&\simeq \frac{3}{2} \ln\left(\frac{M}{1 \text{ amu}}\right) + \frac{5}{2} \ln\left(\frac{T}{300 \text{ K}}\right) - \ln\left(\frac{P}{1 \text{ bar}}\right) + 13,
\end{aligned}$$ (7)

where M is mass of the molecule, and the subscript "m" denotes a value per mol. The standard entropy and enthalpy of several molecules are shown in Table 2.

	CH$_4$	H$_2$O	CO$_2$	H$_2$
$S°$ [kJ/mol K]	0.143	0.144	0.156	0.117
$H°$ [kJ/mol]	1656	928	1598	436

Table 2
The standard entropy $S°$ (at $T = 298\,\text{K}$ and $P = 1\,\text{bar}$) for CH$_4$, H$_2$O, CO$_2$, and H$_2$, calculated by Eq. (7). For comparison, the total bond enthalpy $H°$, or the standard enthalpy change for atomization (e.g., H$_2$O $\longrightarrow$ 2 H + O), of these species is also provided, calculated using bond energies from Table1.

Setting the standard pressure $P°$ to 1 bar, $\Delta_\text{r}S°$ is represented as follows;

$$\frac{\Delta_\text{r}S°}{R} = \sum_J \nu_J \frac{S_\text{m}°(J)}{R}$$

$$\simeq \frac{3}{2} \ln\left(\prod_J M_J^{\nu_J}\right) + \left(\sum_J \nu_J\right)\left[\frac{5}{2}\ln\left(\frac{T}{300\,\text{K}}\right) + 13\right]. \tag{8}$$

where J denotes the chemical species and ν_J is the corresponding stoichiometric number. Since the dependence of molecular mass M, P, and T are weak, $\Delta_\text{r}S°$ is generally dominated by the change in total number of molecules.

To summarize, in this study, the weight of probabilities to select the reactions is expressed as follows:

$$W = \begin{cases} \dfrac{k_\text{B}T}{h}\exp\left(\dfrac{\alpha\Delta_\text{r}S°}{R}\right)\exp\left(-\dfrac{\alpha\Delta_\text{r}H° + \beta}{RT}\right)[R_1] & : \text{first-order reaction} \\[3ex] \dfrac{k_\text{B}T}{h}\left(\dfrac{RT}{P°}\right)\exp\left(\dfrac{\alpha\Delta_\text{r}S°}{R}\right)\exp\left(-\dfrac{\alpha\Delta_\text{r}H° + \beta}{RT}\right)[R_1][R_2] & : \text{second-order reaction} \end{cases}, \tag{9}$$

where $[R_1]$ and $[R_2]$ are the molar concentrations of the reactants, derived using Eq.(20). The enthalpy change is characterized by bond energy, while the entropy change is determined by the stoichiometric numbers, masses of the reactants and products, and temperature, as explained above. By incorporating entropy into our model, it has been refined into a more general thermodynamics-based framework, allowing its application to higher-temperature reactions. We discuss the impact of the approximations of reaction rates in Section 4.2.

It should be noted that three-body reactions (e.g., H $\cdot$ + H $\cdot$ + M (third body) $\rightleftharpoons$ H$_2$ + M), which require an additional molecule or atom to either remove excess energy (forward direction in the reaction above) or supply the energy needed for bond dissociation (reverse direction), are not explicitly expressed in the current model. Since the third body does not undergo any change during the reaction, we treat these reactions without considering the third body in our simulations (i.e., the above reaction is treated as H $\cdot$ + H $\cdot$ $\rightleftharpoons$ H$_2$). However, the reaction rates of such reactions depend on the concentration of the third body, which our current model does not account for. Under the high-pressure conditions considered in this study ($10^7 - 10^{11}$ Pa), the concentration of third bodies is expected to be sufficiently high that the reaction rates become effectively independent of their concentration. Furthermore, since the equilibrium composition does not depend on the reaction rates including those of three-body reactions, but is determined by the Gibbs energies of the molecular species, the dependence of reaction rates on third-body concentrations can be neglected under the high-temperature and high-pressure conditions of vapor plumes where equilibrium is achieved. The kinetic model (GRI-Mech 3.0), which we compared our results with in Section 3.1.1, does include this concentration dependence in its calculations. Our model, despite neglecting this factor, remains consistent with the kinetic model (see Section 3.1.1).

2.3. Temperature and pressure change of a vapor plume

In Ochiai et al. (2024), a constant temperature ($\sim 50 - 100\,\text{K}$) was assumed throughout the simulations, with a transition from a UV-irradiated phase to a phase without UV irradiation, representing the sedimentation of an ice dust particle from the upper layer of the protoplanetary disk to the UV-shielded midplane. In contrast, in the case of an asteroid impact, both temperature T and pressure P are extremely high immediately after the impact, rapidly decreasing as the vapor plume undergoes adiabatic expansion.

This section presents the model for the decay of temperature and pressure (T and P) in the impact vapor plume, which are essential parameters for our chemical reaction simulations. In this study, we adopt a fiducial impact case with an impact radius of 0.5 km and an impact velocity of 10 km/s. When an impact occurs, a portion of the impact energy is converted into thermal energy, resulting in a temperature increase. The specific impact energy with the impact velocity v is given by:

$$E_{\mathrm{imp}} = \frac{1}{2}v^2 = 50 \left(\frac{v}{10 \,\mathrm{km/s}} \right)^2 \,\mathrm{km^2/s^2}. \tag{10}$$

The specific thermal energy is represented as $c_P T$, where c_P is specific heat of the substances. With the heat conversion rate ϵ, the post-impact temperature rise is expressed as:

$$T_0 \sim \frac{\epsilon E_{\mathrm{imp}}}{c_P} \sim 5 \times 10^3 \left(\frac{\epsilon}{0.1} \right) \left(\frac{v}{10 \,\mathrm{km/s}} \right)^2 \left(\frac{c_P}{10^3 \,\mathrm{J/kg \cdot K}} \right)^{-1} \,\mathrm{K}. \tag{11}$$

To fit the temperature estimated from Eq. (11) with the results of Marchi et al. (2013), which showed post-impact temperatures using the two-dimensional hydrocode; impact-Simplified Arbitrary Lagrangian Eulerian (iSALE), we adopt $\epsilon = 0.1$. Consequently, the initial temperature of a vapor plume is set to 5000 K in this study.

To estimate the initial pressure of the impact vapor plume P_0, we use Hugoniot relation, as follows:

$$P_0 \simeq \rho U_s u_p \simeq \rho(C_{\mathrm{imp}} + S_{\mathrm{imp}} u_p) u_p, \tag{12}$$

where ρ is pre-shock density of the impactor, U_s is the shock-wave velocity, u_p is the particle velocity, C_{imp} is the bulk sound velocity of the impactor material, and S_{imp} is a material constant. For simplicity, assuming the impactor and target are made of the same material, the particle velocity of the impactor is expressed as $u_p = (1/2)v$ as the impactor and the target have the same pressure and the same velocity at the boundary surface after the impact. Furthermore, assuming basalt as the material, and using the values for basalt presented in Sekine et al. (2008), $\rho = 2.70 \,\mathrm{g/cm^3}$ $C_{\mathrm{imp}} = 3.5 \,\mathrm{km/s}$ and $S_{\mathrm{imp}} = 1.3$, we obtain $P_0 \simeq 140 \,\mathrm{GPa}$.

Next, we derive the time variations of temperature and pressure in an impact vapor plume that adiabatically expands. Although a realistic vapor plume is a hemisphere, we estimate the T-P variations assuming the spherically symmetric vapor plume, for simplicity. Given the expansion velocity (radial velocity) of the vapor plume as the sound speed, the radius of the vapor plume r_{vp} evolves as follows:

$$\frac{dr_{\mathrm{vp}}}{dt} = c_s \simeq 1.7 \left(\frac{T}{10^4 \,\mathrm{K}} \right)^{1/2} \left(\frac{\mu}{30} \right)^{-1/2} \,\mathrm{km/s}, \tag{13}$$

where μ is the mean molecular weight of the vapor. Using the normalized quantities; $\tilde{r}_{\mathrm{vp}} = r_{\mathrm{vp}}/r_{\mathrm{imp}}$ and $\tilde{T} = T/T_0$, where r_{imp} is the impactor radius (approximately the initial vapor plume's radius) and T_0 is the initial vapor plume temperature, the above equation is rewritten as follows:

$$\frac{d\tilde{r}_{\mathrm{vp}}}{dt} \simeq C\tilde{T}^{1/2} \,;\, C = 3.3 \left(\frac{r_{\mathrm{imp}}}{0.5 \,\mathrm{km}} \right)^{-1} \left(\frac{T_0}{10^4 \,\mathrm{K}} \right)^{1/2} \left(\frac{\mu}{30} \right)^{-1/2}. \tag{14}$$

Assuming adiabatic expansion of ideal gas, $\tilde{r}_{\mathrm{vp}} \simeq \tilde{T}^{-1/3(\gamma-1)}$, where γ is the adiabatic exponent. Substituting the this relation into Eq. (14),
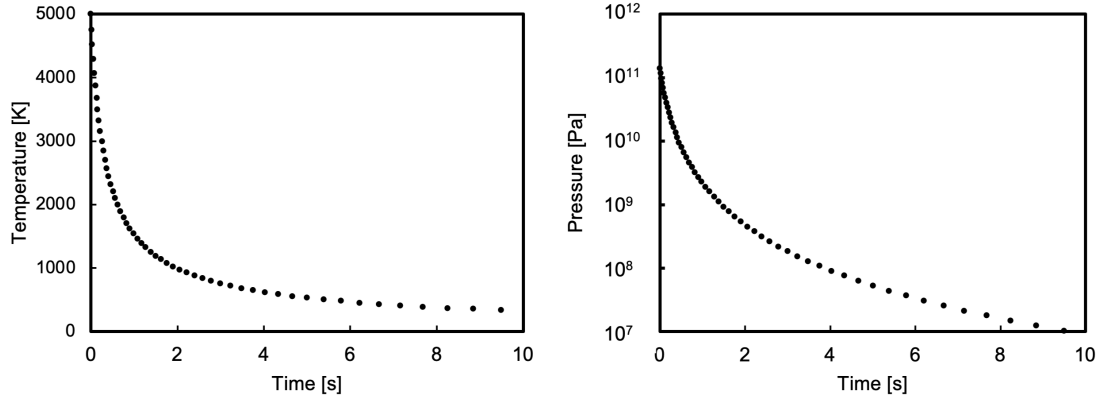
$$\frac{d\tilde{T}}{dt} \simeq -3(\gamma - 1)C\tilde{T}^{\frac{1}{3(\gamma-1)}+\frac{3}{2}}. \tag{15}$$

By solving this equation, we obtain the temperature variation, and the pressure variation can be determined using the relation between $\tilde{T}$ and $\tilde{P}(= P/P_0)$, as follows:

$$\tilde{P} = \tilde{T}^{\gamma/(\gamma-1)}. \tag{16}$$

In this study, we use $\gamma = 1.4$ as a constant value.

Figure 2: Typical time evolution of temperature and pressure in impact vapor plume assumed in this study. Initial temperature and pressure are 5000 K and 140 GPa, respectively. Each point represents a 5% change in temperature calculated from Eq. (15) and Eq. (16), using $C = 2.3$ and $\gamma = 1.4$.

2.4. Coupling method

Based on Eq. (15), the cooling time scale over which the temperature changes by 5% is calculated as

$$t_{\text{cool}} = \left| \frac{0.05\tilde{T}}{d\tilde{T}/dt} \right| = \frac{0.05}{3(\gamma - 1)C} \tilde{T}^{-\frac{1}{3(\gamma-1)} - \frac{1}{2}} \text{ s.} \tag{17}$$

For $\gamma \sim 1.4$ and $\mu \sim 30$,

$$t_{\text{cool}} \sim 0.01 \left(\frac{r_{\text{imp}}}{0.5\,\text{km}} \right) \left(\frac{T}{10^4\,\text{K}} \right)^{-1/2} \text{ s.} \tag{18}$$

On the other hand, the time step of the i-th reaction step in the Monte Carlo calculation, Δt_i, is expressed as

$$\Delta t_i = \frac{1}{\sum k_{\text{first,i}} + C_i \sum k_{\text{second,i}}} \text{ s,} \tag{19}$$

where C_i is the concentration calculated as

$$C_i = \frac{P_i/RT_i}{N_{\text{molecules,i}}}, \tag{20}$$

and $N_{\text{molecules,i}}$ is the total number of molecules in the molecular set at the i-th step (see Appendix B for more details), and $\sum$ indicates the sum of $k_{\text{first,i}}$ and $k_{\text{second,i}}$ for all reaction candidates at the i-th step.

At each step of the reaction calculation, the weights of reaction probabilities (Eq. (9)) are calculated using the input temperature and pressure, and the cumulative reaction time is obtained by summing Δt_i. In this study, to couple the reaction calculation with the temperature and pressure changes, the temperature and pressure are updated when the elapsed reaction time since the last temperature and pressure update exceeds t_{cool}. When the update occurs, T is reduced by 5%, and P is recalculated using Eq. (16) with the new T. At the same time, t_{cool} is updated using the new T and the mean molecular weight μ derived from the molecular set at that step (Eq. (17)). Consequently, the chemical reaction calculations utilize step-wise T-P functions, with temperature reduced by 5% increments and the corresponding decrease of pressure. Figure 2 shows the typical time evolution of temperature and pressure in an impact vapor plume used in the current calculations.

In the initial high-temperature phase, since Δt_i is extremely small, the system reaches equilibrium in a time much shorter than t_{cool}. Therefore, to reduce computational cost, the maximum number of reaction steps at a given temperature is set to 10^5 steps, which is large enough for the current simulation set to reach equilibrium. Once this number is reached, the simulation transitions to the next temperature state.

type	atomic composition	C/H	O/H
LL (ordinary chondrite)	50 H, 12 C, 4 N, 20 O	0.24	0.40
CI (carbonaceous chondrite)	50 H, 7 C, 4 N, 37 O	0.14	0.74
EL (enstatite chondrite)	12 H, 22 C, 4 N, 25 O	1.83	2.08
comet	42 H, 12 C, 2 N, 21 O	0.29	0.50

Table 3
Atomic compositions for CI, LL, and EL chondrite types. The comet type is used for the comparison with Ishimaru et al. (2010) (see Section 3.1.1). The number of atoms represents those included in a single molecular set of each simulation. These ratios between H, C, N, and O are determined based on the equilibrium compositions at 1500 K and 100 bar derived in Schaefer and Fegley (2010). We assumed mixing of 5% by volume of the ambient N_2 atmosphere into the vapor plume and increased the N fraction.

2.5. Initial conditions

For impactor materials, we assume three types of chondrites; carbonaceous, ordinary, and enstatite chondrites. We calculate chemical reactions among only volatiles (C, H, N, and O species), assuming specific elemental compositions to each material. Under high temperatures immediately after an impact, vaporization of rock components also occurs and they condense out during cooling. The condensation of these components can trap volatile elements, possibly leading to the change in elemental compositions of the gas phase over time. However, the kinetics of these processes are not clear at the moment. Thus, we ignore this effect based on the assumption that the condensation mostly completes at sufficiently high temperature.

Schaefer and Fegley (2010) focused on impact outgassing and calculated the equilibrium compositions in gas phase from chondrite compositions. We determine the elemental compositions of our calculations based on the equilibrium gas composition of CI (carbonaceous chondrites), LL (ordinary chondrites), and EL (enstatite chondrites) chondrites at 1500 K and 100 bar calclulated in Schaefer and Fegley (2010). While this temperature and pressure condition is different from the initial condition assumed in this study, they showed that the compositions of the nominal condition (1500 K and 100 bar) are still valid at other temperatures and pressures. These compositions also contain trace amounts of sulfur; however, sulfur is ignored in this study as its abundance is sufficiently small compared to C, N, O, and H. Furthermore, in this study, mixing with nitrogen atmosphere was assumed as in previous experiments and the nitrogen ratio was increased from the equilibrium compositions in Schaefer and Fegley (2010). Although it is currently unclear whether and how an impact vapor plume mixes with the surrounding atmosphere, we assumed that 5% of total impact vapor volume come from pure N_2 atmosphere, representing the early Earth's atmosphere. The elemental compositions and the corresponding initial sets of molecules used in this study are shown in Table 3.

Initial temperature and pressure of the impact vapor plume are 5000 K and 140 GPa, respectively as described in Section 2.3. However, since quench temperature is expected to be sufficiently lower than 5000 K, we start the chemical reaction calculations from 3000 K. The results from our calculations and Ishimaru et al. (2010) both showed that 3000 K is high enough for the gas phase reactions in vapor plumes to reach the equilibrium states (see Section 3.1.1). The simulation is terminated when the temperature falls below 300 K, typically lasting for 10 seconds in the case of $r_{imp} = 0.5\,km$.

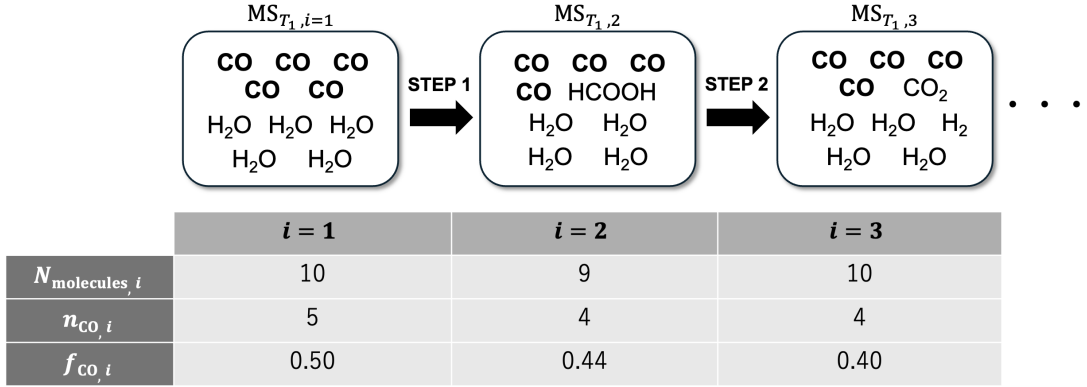## 2.6. Evaluation of mole fractions

Here, we describe the method to evaluate mole fractions based on molecular sets and reaction sequences obtained in this chemical reaction simulation. Let $N_{molecules,i}$ be the total number of molecules in the molecular set before the i-th reaction happens, and let $n_{A,i}$ be the number of molecules of a chemical species A in the same set. The mole fraction of A at this step is given by $f_{A,i} = n_{A,i}/N_{molecules,i}$ as shown in Fig. 3.

However, in this study, for computational reasons, we calculate the mole fraction representative of each temperature rather than for each individual step. Since the calculations at each temperature consist of multiple steps, the representative mole fraction for a given temperature is taken as a weighted average, accounting for the differences in reaction time Δt_i across reaction steps.
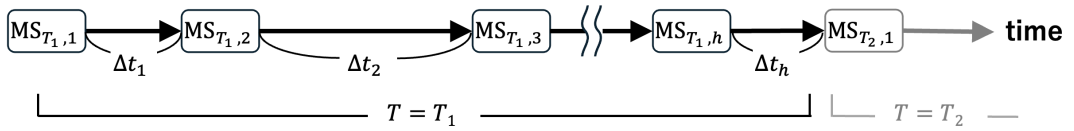
At $T = T_1$, this weighted average of the mole fractions, $F_A(T_1)$, is expressed as:

$$F_A(T_1) = \frac{\sum_{i=1}^{n}(\Delta t_i f_{A,i})}{\sum_{i=1}^{n}(\Delta t_i)}, \tag{21}$$

Figure 3: Schematic diagram of a reaction sequence at $T = T_1$. In this figure, MS, $N_{\text{molecules,i}}$, $n_{\text{CO,i}}$, $f_{\text{CO,i}}$ represent "Molecular Set", the number of molecules in the molecular set, and the number of CO molecules and the mole fraction of CO, respectively.

where $f_{A,i}$ is the mole fraction of species A at the i-th step, n represents the total number of reaction steps at $T = T_1$. As described in Section 2.4, the temperature is reduced by 5 % with each update, starting at 3000 K in this study. At each temperature, the mole fraction of the species of interest is calculated using Eq. (21). Since this Monte Carlo simulation consists of multiple independent trials generated with different random number seeds, as mentioned in Section 2.1, the mole fractions at each temperature are finally averaged across the individual reaction sequences obtained from these trials.

3. Results

3.1. Time evolution of mole fractions of major species

First, we focus on the time evolution of mole fractions of the typical major species–H_2, H_2O, CO_2, CO, CH_4, N_2, and NH_3–to illustrate the general trends in composition evolution and to confirm the consistency of our results with the results obtained by the previous work (Ishimaru et al., 2010).

3.1.1. Comparison with a previous study on cometary impact

Although comparing our results with experimental studies would be a valuable way to validate the simulations, experimental data are often not sufficiently quantitative or comprehensive to justify theoretical models. Therefore, in this subsection, we compare our simulation results with those obtained using a different theoretical approach–a kinetic model–which provides a useful benchmark for major molecular species.

Ishimaru et al. (2010) simulated impact-induced chemical reactions using a kinetic model (GRI-Mech version 3.0) based on a predefined reaction network, but only for a cometary impact case. While the present study focuses on asteroidal (rocky-body) impacts, kinetic model simulations for such cases have not yet been published. Accordingly, we adopt a cometary composition in this subsection to enable direct comparison with the results of Ishimaru et al. (2010).

While the validity of GRI-Mech 3.0 for combustion processes has been demonstrated through comparisons with experimental data, our results, as shown later, demonstrate the synthesis of minor products not included in GRI-Mech 3.0 that could play an important role in amino acid synthesis. This is because, unlike kinetic models, our Monte
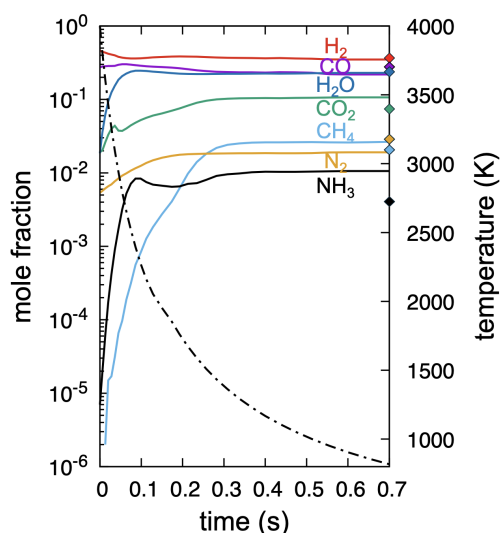
Figure 4: Time evolution of mole fractions of major species (H_2, H_2O, CO_2, CO, CH_4, N_2, and NH_3; solid lines, left axis) and temperature (dot-dashed line, right axis) for a cometary impact. Diamonds on the right axis represent the mole fractions of each species in the quenched composition obtained in the previous study (Ishimaru et al., 2010) (thier Fig. 6). The atomic composition used is shown in Table 3 (comet type). The initial temperature and initial pressure are 4000 K and 30 GPa, respectively, corresponding to the conditions in Ishimaru et al. (2010). The value of β in Eq. (5) is set to 300 kJ/mol.

Carlo simulation considers all possible reactions, enabling the synthesis of chemical species excluded from the kinetic model. It should be noted that, species with low abundance and/or small impact on the reaction network of the targeted chemical process are usually omitted from kinetic models.

Nevertheless, since such minor chemical species have little effect on the major composition, our results for the evolution of the major species should be consistent with those of Ishimaru et al. (2010). The prediction of the mole fraction evolution for the major species of the cometary composition (Table 3) with our Monte Carlo method is shown in Fig. 4. The quenched composition of the seven major products is consistent with Ishimaru et al. (2010) (their Fig. 6), although some deviations are observed in the early evolution of H_2O, CH_4, and NH_3 at temperatures around 4000–2000 K. These deviations are likely due to approximations in the Gibbs energy (approximations in enthalpy and entropy changes), but do not significantly affect the quench process, which occurs at lower temperature ($\sim$ 1000 K). Thus, Figure 4 supports the validity of our method in capturing overall compositional trends, rather than accurately predicting the exact abundances of individual species. We also note that, due to the limited information provided in Ishimaru et al. (2010), the T-P path used in our calculation for Fig. 4 may not fully replicate theirs, potentially contributing to the observed deviations.

While this calculation focuses on a cometary impact, comparisons with kinetic model calculations for chondritic compositions, which are the assumed impactor compositions in this study, are also essential. Preliminary results from such calculations (Miyawaki and Genda, in preparation) demonstrate consistency with our Monte Carlo simulations across CI, LL, and EL compositions. Building on the agreement between our Monte Carlo method and the kinetic model for these results for major species mole fractions, we extend this approach to investigate the major species generated by a rocky body impact.
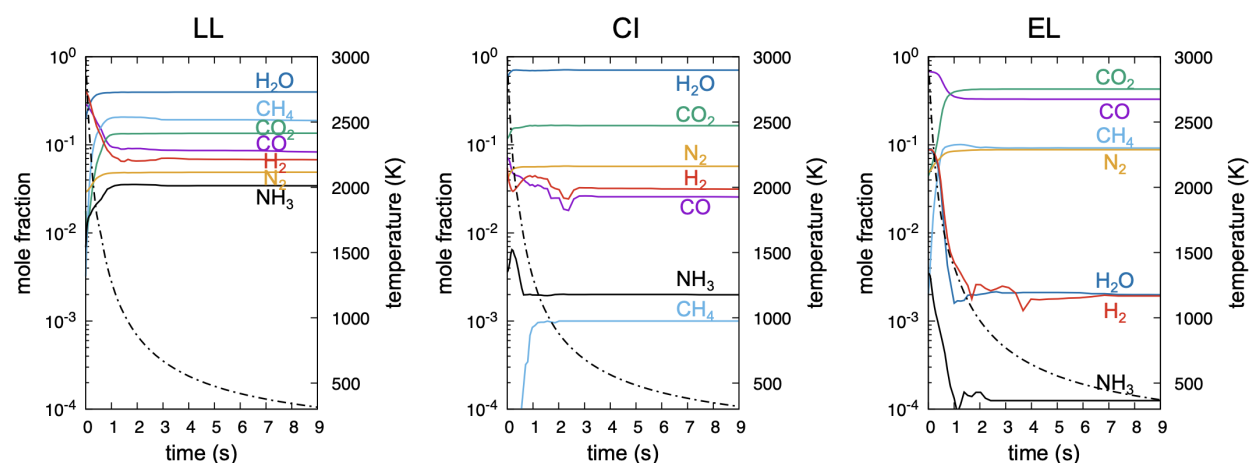
3.1.2. Results for CI, LL, and EL chondritic compositions

Figure 5 shows post-impact time evolution of mole fractions of the major chemical species obtained from the CI, LL, and EL chondritic compositions. Regarding the C/H and O/H ratios of each impactor composition shown in Table 3, CI (C/H = 0.14, O/H = 0.74) and LL (C/H = 0.24, O/H = 0.40) are similar, with CI being slightly oxidizing. In contrast, the EL composition (C/H = 1.83, O/H = 2.08) differs significantly, being H-poor and extremely C-rich. We note that, as these compositions are the equilibrium compositions of degassed volatiles at 1500 K and 100 bar, they represent different redox states from the bulk compositions.

Figure 5 shows the composition changes cease almost entirely below around 1000 K due to quenching. Both the LL and CI compositions result in H_2O-rich gas, but in the LL-type, CH_4 and CO_2 become the next most abundant species, except for the high-temperature region (3000 − 2500 K), where H_2 and CO are dominant. On the other hand, in the more oxidizing CI composition, CO_2 becomes the second most abundant species, while the fraction of CH_4 is about two orders of magnitude lower than that in the LL-type.

In the EL composition, CO_2 and CO become the dominant components after the initial high-temperature region (3000−2500 K), where CO, H_2, and H_2O are prevalent. Despite its very high O/H ratio, CH_4 is also relatively abundant ($F_{CH_4} \sim 0.1$). These characteristics of the EL-type are attributed to its C-rich composition.

For N-bearing species, the mole fraction of N_2 is similar across the three compositions ($F_{N_2} \sim 0.1 − 0.01$) and is always the dominant N-species in their quenched compositions. In contrast, the mole fraction of NH_3 decreases significantly (by up to two orders of magnitude) in the order of LL, CI, and EL compositions, corresponding to the O/H ratio trend. As will be discussed in Section 3.2.2, NH_3 is an essential molecule for many biomolecular synthesis pathways. The strong dependence of its mole fraction on impactor composition can suggest the importance of NH_3 production as a key process in biomolecular synthesis within impact vapor plumes.

Figure 5: Time evolution of mole fractions of major species, $H_2, H_2O, CO_2, CO, CH_4, N_2$, and NH_3 (solid lines) and temperature (dot-dashed line), obtained from the CI, LL, and EL chondritic compositions. The initial condition of the impact vapor plume is $T_0 = 5000$ K and $P_0 = 140$ GPa. Note that the calculations are started from 3000 K ($t = 0$) as explained in Section 2.5. The value of β in Eq. (5) is set to 300 kJ/mol.

3.1.3. Dependence on the model parameter β

Figure 6 shows the change in mole fractions of major species in the LL composition, calculated with different values of β, the parameter to evaluate the Gibbs energy of activation in Eq. (5). As Eq. (9) indicates, the larger the β is, the smaller the estimated reaction rate constants are (i.e., the slower the reactions are). Therefore, the choice of β influences the overall reaction rates in the simulations.

On the other hand, equilibrium composition is determined by $\Delta_r G$ and is independent of β (see Appendix A). Thus, in the high-temperature region where the equilibrium is reached, the compositions remain the same regardless of the β value, as shown in the very early evolution ($\sim 3000 − 1500$ K) in Fig. 6.

Since the cooling timescale is also independent of β (Eq. 17), increasing β slows down the reaction rates without changing how quickly the system cools. As a result, reactions are quenched earlier (at higher temperatures) when β is large, because the slower reactions can no longer keep up with the cooling. In contrast, when β is smaller, reactions proceed more quickly and continue to evolve even at lower temperatures before being quenched. This allows the composition to shift further, following equilibrium trends associated with decreasing temperature (e.g., $2\,CO + 2\,H_2 \rightleftharpoons CH_4 + CO_2$).

Nevertheless, within the range of β values assumed in this study ($\beta = 250$–350 kJ/mol), these effects do not substantially alter the major components of the quenched composition. Therefore, the influence on the abundance of other products, including organic compounds discussed in the following sections, is also considered minimal. Although
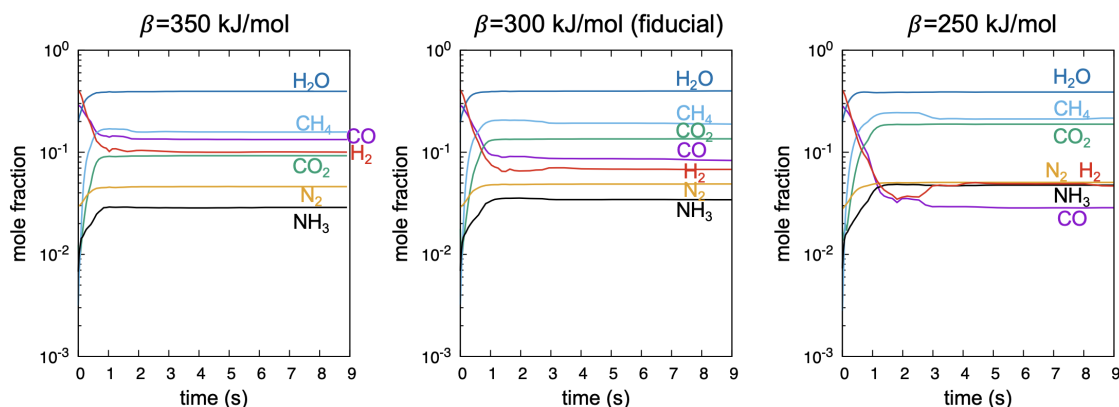
Figure 6: Time evolution of mole fractions of major species obtained from the LL-type composition using β =250, 300, and 350 kJ/mol. The value of β influences the estimation of the standard Gibbs energy of activation (Eq. (5)), and consequently, the overall reaction rates (Eq. (9)) in this study. All other calculation settings are identical to those used in Fig. 5.

we focus only on the dependence on α in this study, changing the value of α would have a similar effect, as it influences only the reaction rates and quench temperature but not the equilibrium composition.

3.2. Biomolecules synthesis in impact vapor plumes

In Ochiai et al. (2024), the previous version of our previous Monte Carlo simulation showed that amino acids and sugars are synthesized by UV irradiation under cryogenic conditions (with $T \sim 50 - 100$ K), corresponding to the surface of icy grains in a protoplanetary disk. We also investigated how the synthesis efficiencies of amino acids and sugars depend on the initial atomic ratios of the ice composition, specifically the C/H and O/H ratios.

In contrast, the present simulations do not yield significant mole fractions of amino acids and sugars. This is because these compounds are thermodynamically unstable at high temperatures and decompose rapidly, even if they are episodically formed. However, as shown in the following sections, our results show that a sufficient variety of precursors necessary for the formation of biomoecules, such as amino acids, sugars, and nucleobases, are synthesized and remained in the quenched compositions. Notably, some of these precursors are absent in the previous reaction network used by Ishimaru et al. (2010), meaning that they cannot be produced within that framework. We first present the results on the synthesis of organic molecules, including biomolecules' precursors (Secttion 3.2.1) and then discuss how biomolecules are synthesized in impact vapor plumes (Section 3.2.2).

3.2.1. Synthesis of organic molecules

Figure 7 shows the time evolution of mole fractions of organic molecules produced in the post-impact reactions of the LL, CI, and EL compositions. We note that the species plotted are not necessarily all organic products but those found to be relatively abundant among about 30 relevant organic molecules examined. Although isocyanic acid (HNCO) is classified as inorganic compounds, they are also plotted in Fig. 7 because of their structural similarities to organic molecules.

In the LL chondritic composition, a variety of organic molecules are produced. The major species among them are hydrogen cyanide (HCN), formalydehyde (CH_2O), methanimine (CH_2NH), and ethane (C_2H_6). Other products include methanol (CH_3OH), acetaldehyde (CH_3CHO), ethanimine (CH_3CHNH), N-methylmethanimine (CH_3NCH_2), formic acid (HCOOH), formamide (NH_2CHO), acetonitrile (CH_3CN), and isocyanic acid (HNCO). As these products suggest, nitrogen-containing organic compounds are produced more diversely and abundantly in the LL type compared to the other two types, enabling the synthesis of species like formamide, which is absent in the other two compositions.

The EL chondritic composition generates organic compounds that are somewhat similar to those produced by the LL composition. The most abundant species is HCN, and the fractions of all other products–methane (C_2H_6), methanimine (CH_2NH), formalydehyde (CH_2O), acetonitrile (CH_3CN), acetaldehyde (CH_3CHO), isocyanic acid (HNCO), ethanimine (CH_3CHNH), N-methylmethanimine (CH_3NCH_2), propane (C_3H_8), and formyl cyanide (CHOCN)–are approximately one order of magnitude, or even more, lower than that of HCN. Despite its high O/H ratio,
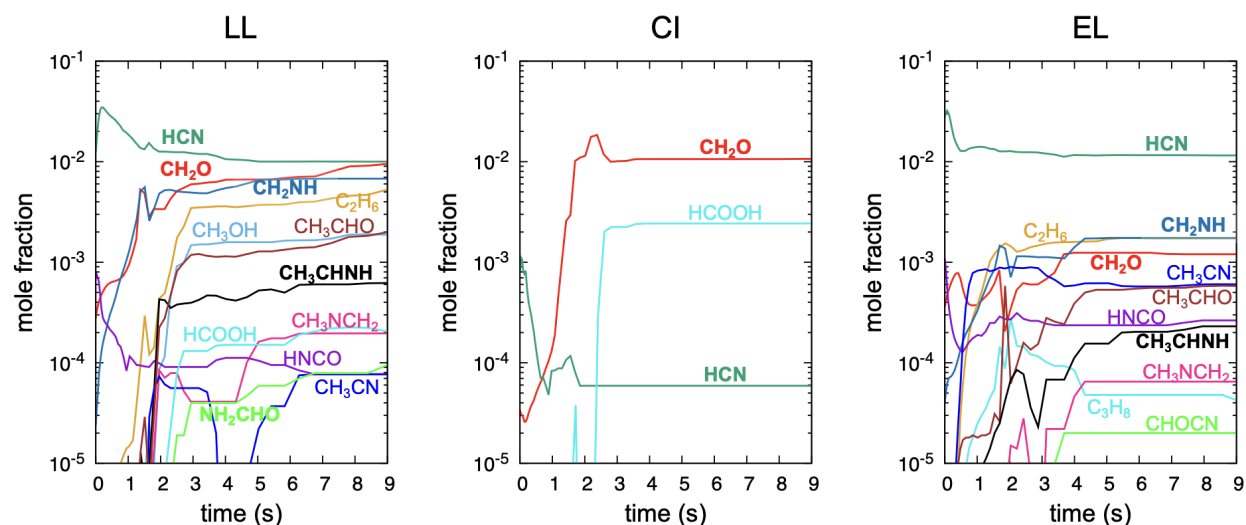
Figure 7: Time evolution of mole fractions of organic molecules. The molecules represented by each chemical formula are as follows: hydrogen cyanide (HCN), formaldehyde (CH$_2$O), methanol (CH$_3$OH), formic acid (HCOOH), isocyanic acid (HNCO), methanimine (CH$_2$NH), ethanimine (CH$_3$CHNH), N-methylmethanimine (CH$_3$NCH$_2$), acetaldehyde (CH$_3$CHO), acetonitrile (CH$_3$CN), formamide (NH$_2$CHO), formyl cyanide (CHOCN), ethane (C$_2$H$_6$), propane (C$_3$H$_8$). Molecules considered particularly important for biomolecule synthesis (see Section 3.2.2) are indicated with bold lines.

the carbon-rich composition of the EL type promotes organic synthesis, resulting in the relatively abundant formation of a C3 compound (C$_3$H$_8$). Moreover, while the EL type exhibits a significantly low abundance of NH$_3$ among the three compositions (Fig. 5), the efficient production of HCN presumably promotes the synthesis of N-containing organic compounds, including acetonitrile and formyl cyanide.

In the CI composition, only hydrogen cyanide (HCN), formaldehyde (CH$_2$O), and formic acid (HCOOH) are observed with significant fraction, indicating the most limited organic compound production among the three compositions. Compared to the LL type, which has a similar atomic ratio, the CI composition is more C-poor and oxidizing, resulting in a significantly lower production rate of reactive species such as NH$_3$ and CH$_4$. This is likely to inhibit the overall synthesis of organic compounds in the CI composition.

It is worth noting that we confirmed a decrease in the O/H ratio of the vapor composition leads to an increase in the mole fraction of HCN for each impactor material. However, it is also evident that O/H is not the sole factor controlling HCN production, as demonstrated by the fact that the EL composition yields a higher HCN mole fraction than the CI composition, despite having a higher O/H ratio. Other parameters, such as C/N and/or C/O ratios, may also play important roles in regulating HCN formation. Understanding these dependencies requires further study, which is left for future work.

While, in these simulations, we detect a variety of complex organic molecules, including amino acids, particularly at high temperatures (> 1500 K), their concentrations are extremely low. Such complex organic molecules, consisting of a large number of atoms, are thermodynamically unstable and rapidly decompose even if they happen to be synthesized. Many complex organic molecules with extremely short lifetime (on the order of less than 1 nanosecond) have been also observed in AIMD simulations of post-shock chemical reactions at temperatures about 3000–4000 K (Goldman et al., 2010).

We stress that most of the organic compounds identified in this study (Fig. 7) are not included in the reaction network used in the previous study (Ishimaru et al., 2010), and some of them can play crucial roles in biomolecules synthesis. For example, methanimine (CH$_2$NH), produced in the LL and EL compositions, has been proposed as a precursor to glycine (the simplest amino acid) via the Strecker reaction, one of the plausible reaction mechanisms for prebiotic amino acids synthesis. Formamide (NH$_2$CHO) has also been suggested as a key molecule for the prebiotic synthesis of nucleobases (e.g., Saladino et al., 2001). We discuss potential mechanisms for biomolecules synthesis in more detail in Section 3.2.2.
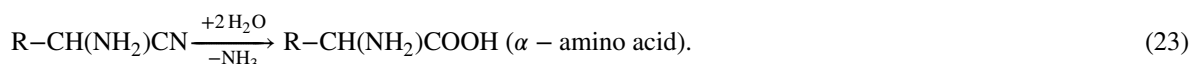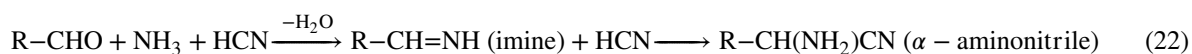
Since GRI-Mech, the chemical kinetic model used in Ishimaru et al. (2010), was primarily designed for modeling combustion processes, it selectively focuses on species and pathways relevant to combustion reactions. As a result, most kinds of trace organic compounds shown in Fig. 7 are not considered in the reaction network of GRI-Mech. Accordingly, Ishimaru et al. (2010) were not able to predict the formation of these compounds. Our results thus provide the first theoretical prediction of diverse organic compound production and the synthesis of precursors to biomolecules in impact vapor plumes that produced by various chondritic materials. This underscores the significance of the Monte Carlo simulation approach, which does not rely on predefined chemical species and reaction pathways, enabling the inclusion of all potential products.

3.2.2. Possible mechanisms for the syntheses of amino acids, sugars, and nucleobases

As mentioned above, the present calculations show that no biomolecules remain in the quenched compositions of impact vapor plumes. However, our results show that several molecules, which serve as starting materials or intermediates in biomolecule synthesis pathways, are abundantly produced. As the temperature of the impact vapor plume decreases, the condensation of H_2O and the dissolution of the reactants of those reactions may allow biomolecule synthesis to proceed in the aqueous solution. While our current model, which focuses on gas-phase chemical reactions, does not account for condensation processes and liquid-phase reactions, we assume the formation of aqueous solutions after quenching and outline the potential biomolecule synthesis pathways based on the products identified in this study.

One such pathway is the Strecker reaction, a potential prebiotic synthesis route for α-amino acids (e.g., Magrino et al., 2021). This reaction involves two main stages: (1) formation of α-amino nitrile from the starting molecules (aldehydes, NH_3, and HCN), and (2) hydolysis of α-amino nitrile to α-amino acid, as follows:

$$R-CHO + NH_3 + HCN \xrightarrow{-H_2O} R-CH=NH \text{ (imine)} + HCN \longrightarrow R-CH(NH_2)CN \text{ }(\alpha-aminonitrile) \tag{22}$$

$$R-CH(NH_2)CN \xrightarrow[-NH_3]{+2H_2O} R-CH(NH_2)COOH \text{ }(\alpha-amino\ acid). \tag{23}$$

Our results indicate that the initial molecules for this reaction–anmonia (NH_3), hydeogen cyanide (HCN), and formaldehyde (CH_2O)–are simultaneously produced in all the compositions (Figs. 5 and 7). Furthermore, our results also show that imine compounds, the intermediates of reaction (22), such as methanimine (CH_2NH) and ethanimine (CH_3CHNH) are produced in impact vapor plumes (Fig. 7), possibly advancing amino acid synthesis. Although Magrino et al. (2021) explored the free energy landscape of each step in the Strecker reaction, including reactions involving imines, the current understanding of how these reactions proceed abiotically remains limited. To clarify the role of imine intermediates in prebiotic amino acid synthesis, further kinetic data and experimental studies under plausible prebiotic conditions will be essential.

While the Strecker reaction can only synthesize α-amino acids, β-amino acids have also been synthesized in shock-recovery experiments (Furukawa et al., 2008, 2015; Takeuchi et al., 2020). The ammonia-involved formose-type reaction, initiated from ammonia and formaldehyde in alkaline conditions, has been proposed as a synthesis pathway for amino acids, including β-amino acids. Our results indicate that both of these starting molecules (CH_2O and NH_3) are synthesized in impact vapor plumes (Figs. 5 and 7), suggesting that amino acids could also be produced through the formose-type reaction. Similarly, such conditions may enable the progression of the formose reaction, which synthesizes sugars through the condensation of formaldehyde (e.g., Breslow, 1959; Briš et al., 2024), implying the potential synthesis of sugars as well.

In the prebiotic synthesis of nucleobases, HCN is a critical starting material. Multiple pathways for nucleobase formation from HCN have been proposed (e.g., Kitadai and Maruyama, 2018, and references therein), including HCN polymerization and reactions with NH_3. Both HCN and NH_3 are detected in all the three compositions, suggesting the potential for nucleobase synthesis in impact vapor plumes. However, the abundances of HCN and NH_3 vary significantly among the compositions: the EL composition is most favorable for HCN, while the LL composition favors NH_3 production. These differences are expected to lead to substantial variations in nucleobase production rates. Additionally, formamide synthesized in the LL composition has been proposed as another important precursor for nucleobase synthesis (e.g., Saladino et al., 2001; Roy et al., 2007), potentially further facilitating their formation. Formamide is detected exclusively in the LL composition, the most reducing among the three and both HCN and NH_3 are found to be abundant in the LL composition compared to the other two. These findings may align with previous experimental results that showed higher nucleobase production in reducing impactor compositions (Furukawa et al., 2015). Further quantitative evaluations of the production rates of these chemical species and parameter surveys using a broader range of compositions will be necessary.

Finally, it should be emphasized that imine compounds, intermediates in the Strecker reaction, and formamide, a potential precursor to nucleobases, were not included in the reaction networks of previous studies. Since our Monte Carlo method does not predefine the reaction network and includes all possible reactions and potential products, our simulation was able to find these compounds. These molecules may be synthesized in relatively high abundances within impact vapor plumes and are critical for understanding the pathways that lead to biomolecule synthesis in such environments.

4. Discussion

4.1. Dependence on impactor size and impact velocity
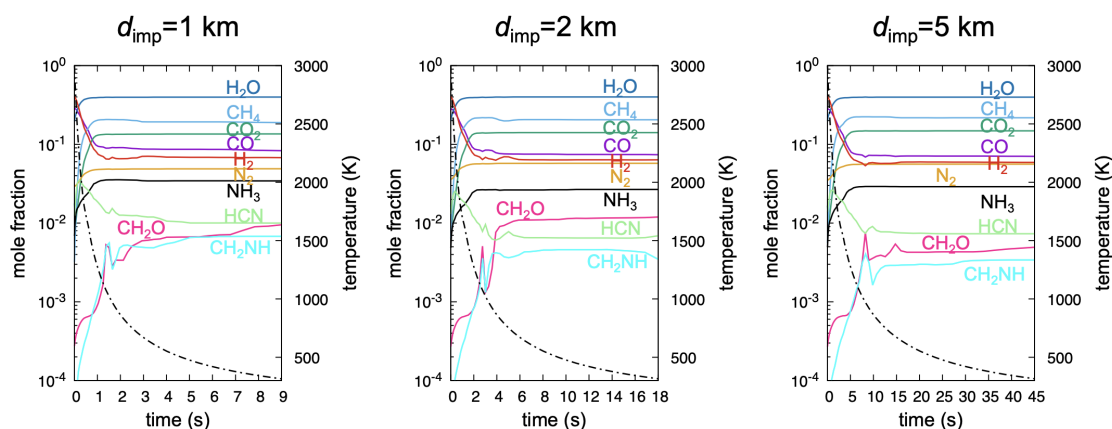
Figure 8: Time evolution of mole fractions of $H_2, H_2O, CO_2, CO, CH_4, N_2,$ $NH_3,$ HCN, $CH_2O,$ CH_2NH (solid lines) and temperature (dot-dashed line), obtained from the LL composition with impactor diameters of 1 km, 2 km, and 5 km.

In this study, we assumed an impactor size of 1 km and an impact velocity of 10 km/s as the fiducial case. Here, to investigate the dependence of the results on these parameters, we focus on the changes in the mole fractions of seven major species ($H_2, H_2O, CO_2, CO, CH_4, N_2,$ and NH_3), as well as three molecules important for biomolecule synthesis (hydrogen cyanide (HCN), formaldehyde (CH_2O), and methanimine (CH_2NH)). Each simulation starts at 3000 K (see Section 2.5), and the value of β in Eq. (5) is set to 300 kJ/mol.

Impactor size, which influences the initial size of the vapor plume and thus the cooling timescale (Eq. (17)), does not significantly affect the results within the examined range of $d_{imp} = 1 - 5$ km as shown in Fig. 8. These results suggest that changes in the cooling timescale associated with the range of impactor sizes have a negligible effect on the quench temperature.

In contrast, impact velocity, which alters the initial temperature (Eq. (11)), pressure (Eq. (12)), and cooling timescale of the plume (Eq. (17)), can have a substantial effect on the vapor plume composition (Fig. 9). Lower impact velocities result in higher pressures at a given temperature, which generally facilitates the formation of larger molecules. For the LL and EL compositions, higher impact velocities lead to notable increases in H_2 and CO, accompanied by decreases in CH_4, HCN, NH_3, and methanimine. The mole fraction of CH_2O increases with impact velocity in the LL case, whereas the clear trend is not found in the EL case. The CI composition remains largely unchanged across different impact velocities, except for the drastic decease in CH_4, NH_3, and HCN.

These results indicate that the dependence on impact velocity varies significantly depending on the initial composition and the molecular species formed. From the perspective of biomolecule synthesis, lower-velocity impacts are expected to be generally more favorable, as they yield higher molar fractions of NH_3, HCN, and methanimine.

4.2. Possible influence of approximations on simulation results

In this study, several approximations were made in evaluating reaction rates. The dependence of reaction rates on third-body concentrations are assumed to be negligible under the impact vapor plume conditions, as mentioned in Section 2.2. The catalytic effects of solid components will also be discussed in Section 4.3.
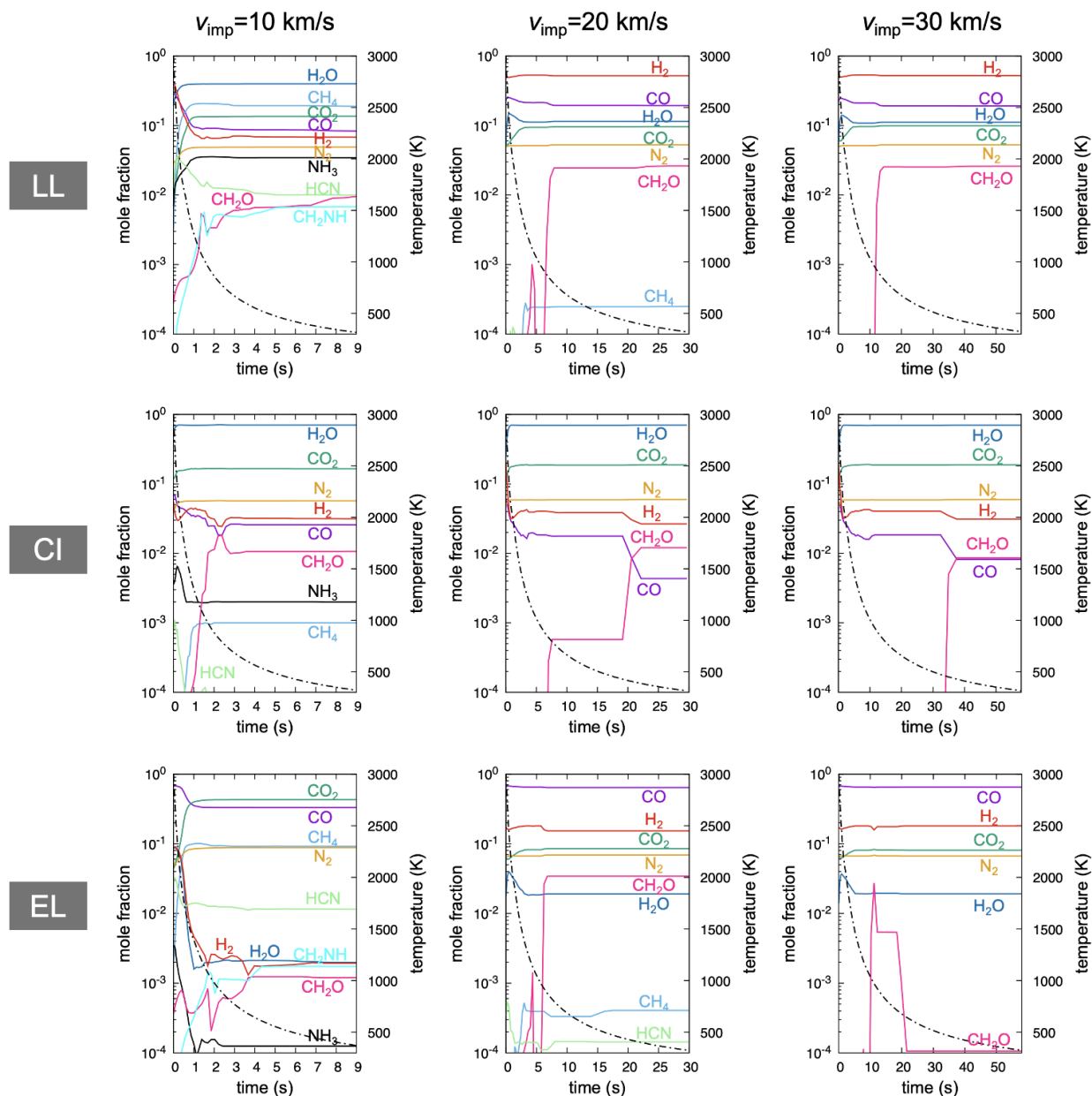
Figure 9: Time evolution of mole fractions of $H_2, H_2O, CO_2, CO, CH_4, N_2$, NH_3, HCN, CH_2O, CH_2NH (solid lines) and temperature (dot-dashed line), for impact velocities of 10 km/s, 20 km/s, and 30 km/s.

Equilibrium composition, which is determined by the Gibbs energy of the system, does not depend on individual reaction rates. Thus, the uncertainties of our results in high-temperature regions where equilibrium is achieved arise from only approximations for enthalpy change and entropy change. Among the cases examined, enthalpy changes show maximum discrepancies of several tens of kJ/mol, while entropy differences remain within 20 J/mol·K[1]. Such discrepancies can lead to inaccuracies in the relative mole fractions among products. However, for the formation of

---

[1]A comparison was made between standard reaction enthalpies and entropies at 300 K calculated using GRI-Mech 3.0 data and those estimated by our model. For example, in the reaction $N_2 + 3H_2 \longrightarrow 2NH_3$, the enthalpy difference is 37 kJ/mol and the entropy difference is 14 J/mol·K. In $CH_3OH \longrightarrow CO + 2H_2$, the enthalpy difference is 29 kJ/mol and the entropy difference is 11 J/mol·K. In $CH_2O + H_2 \longrightarrow CH_3OH$, the enthalpy difference is 38 kJ/mol and the entropy difference is 6 J/mol·K.

organic molecules in impact vapor plumes–the focus of this study–the influence of such errors in the enthalpy and entropy of individual molecules should be small since our model successfully reproduces the general trends in enthalpy and entropy differences between simple molecules and large molecules, as well as the temperature dependence.

While equilibrium composition is determined solely by the Gibbs energy, the quenching process depends also on reaction kinetics. In this study, reaction rates are estimated based on the Eyring equation (Eq. (3)), and the value of the standard Gibbs energy of activation $\Delta^{\ddagger}G^{\circ}$, which predominantly determines the reaction rates, contains uncertainty due to the parameters α and β used in its estimation (Eq. (5)). While these parameter uncertainties do not impact the equilibrium composition itself, they influence the reaction rate and, consequently, the timing of quenching, as described in Section 3.1.3. Furthermore, many of the rate constants used in the kinetic model (GRI-Mech 3.0) employed by Ishimaru et al. (2010) deviate from the Eyring equation. As a result, we found that the empirical rate constants used in GRI-Mech 3.0 sometimes differ significantly from those predicted by our model, depending on temperature. Nevertheless, the overall consistency between our results and the kinetic model may be attributed to the fact that the equilibrium composition at high temperatures is independent of reaction rates, and that the final quench composition is largely determined by this high-temperature equilibrium state.

We emphasize that this simulation is not intended to accurately predict the production rates of individual molecules. Importantly, the various organic compounds observed in this study are challenging to assess using conventional methods, highlighting that this approach–while compromising some level of accuracy–has enabled the investigation of such diverse product distributions.

4.3. Effects of rock-forming elements

In the current simulations, we ignored rock-forming elements such as Si, Al, Cl, Fe, Mg, Ni and others. While their effects on the gas-phase composition of impact vapor plumes is partly taken into account when setting the initial conditions (see Section 2.5), some rock-forming elements may catalyze specific chemical reactions (Shimamura et al., 2019, 2016). Catalysts, which reduce activation energies and accelerate the reactions, should not have any effects to the chemical compositions in high temperature region since the reaction rates are fast enough to reach equilibrium compositions. However, the presence of catalyst would become important when quenching starts to occur, i.e., the reaction timescale and cooling timescale become comparable.

Shimamura et al. (2019) and Shimamura et al. (2016) investigated shock-induced reactions triggered by meteorite impacts using AIMD simulations. They suggested that the adsorption of simple carbon and nitrogen species on meteoritic iron efficiently promotes the formation of C-H bonds and NH_3, which are important for organic synthesis, via processes similar to the Fischer–Tropsch process. Experimental studies have also reported the efficient production of CH_4 from CO and H_2 by Fischer-Tropsch catalysis at around $T = 500 - 600$ K and $P \lesssim 1$ bar (Sekine et al., 2005), which could promote further organic synthesis. However, a previous study simulating a cometary impact (Martins et al., 2013) reported that volatile components alone could produce amino acids, supporting our prediction that amino acids can be synthesized without the catalytic action of metal components.

5. Conclusion

In this study, we investigated the chemical reactions occurring within the impact vapor plume generated by an asteroid impact on early Earth. Focusing on biomolecules synthesized in previous impact simulation experiments (e.g., Furukawa et al., 2008, 2015; Takeuchi et al., 2020), we aimed to elucidate the organic synthesis processes taking place in the impact vapor plume.

To comprehensively explore the complex chemical pathways involved in organic molecule synthesis, we employed a chemical reaction simulation using Monte Carlo method, developed in our previous work (Ochiai et al., 2024). This approach enables the inclusion of all possible reaction pathways without relying on a predefined reaction network by estimating reaction rates based on approximate Gibbs energy changes for each reaction. Additionally, to account for the rapid changes in temperature and pressure due to the adiabatic expansion of the vapor plume after an impact, we developed a method to couple temperature and pressure changes with chemical reaction calculations.

We performed chemical reaction simulations of impact vapor plumes using three different impactor compositions: LL, CI, and EL types. The results showed that a wide variety of organic molecules was synthesized, with the specific types and abundances varying significantly depending on the impactor material (LL, CI, and EL types). Importantly, these organic products include key precursor molecules essential for the formation of biomolecules such as amino

acids, sugars, and nucleobases. This suggests that asteroid impacts on early Earth may have played a critical role in providing the building blocks of life.

However, throughout the post-shock reactions, the concentrations of biomolecules themselves remained extremely low, suggesting that biomolecule synthesis does not occur directly through gas-phase reactions within impact vapor plumes. Instead, our results support a scenario in which precursor molecules synthesized in the gas phase are subsequently concentrated in aqueous solutions following the condensation of H_2O gas as the plume cools. Within these aqueous environments, these precursors may undergo further reactions, such as the Strecker reaction or the formose-type reaction, ultimately leading to the formation of biomolecules. Notably, among these precursor molecules, imine compounds and formamide were absent in the reaction network used in Ishimaru et al. (2010), and their synthesis was theoretically predicted here for the first time. In order to theoretically investigate synthesis of low-abundance complex organic molecules including biomolecules, it is essential to compare kinetic models with non-predefined reaction network approaches, such as our Monte Carlo model, as well as to compare theoretical studies with experiments.

While various environments, such as the atmosphere and hydrothermal vents, have been proposed as sites for the formation of biomolecules and their precursors, our results show that impacts can also generate a wide range of organic compounds, including key precursors for biomolecule synthesis. Although we do not claim that impact vapor plumes are the most favorable setting for biomolecule synthesis, our results highlight their possible contribution and provide a basis for comparison with other origin-of-life scenarios.

In addition, while we assumed mixing of the impact vapor plumes with a pure nitrogen atmosphere, the effect of atmospheric composition on the organic synthesis in impact vapor plumes is limited under low atmospheric mixing conditions in this study. This implies that our results may be applicable to a variety of planets and moons beyond Earth. Although further investigation is required, our findings support the possibility that impact-induced synthesis of biomolecular precursors–and potentially biomolecules themselves–may have occurred on other bodies as well.

6. Acknowledgments

References

Atkins, P., De Paula, J., Keeler, J., 2017. Atkins' physical chemistry. 11 ed., Oxford University Press, London, England.

Bar-Nun, A., Bar-Nun, N., Bauer, S.H., Sagan, C., 1970. Shock synthesis of amino acids in simulated primitive environments. Science 168, 470–473.

Bottke, W.F., Norman, M.D., 2017. The late heavy bombardment. Annu. Rev. Earth Planet. Sci. 45, 619–647.

Breslow, R., 1959. On the mechanism of the formose reaction. Tetrahedron Lett. 1, 22–26.

Briš, A., Baltussen, M.G., Tripodi, G.L., Huck, W.T.S., Franceschi, P., Roithová, J., 2024. Direct analysis of complex reaction mixtures: Formose reaction. Angew. Chem. Int. Ed Engl. 63, e202316621.

Fegley, Jr, B., Prinn, R.G., Hartman, H., Watkins, G.H., 1986. Chemical effects of large impacts on the earth's primitive atmosphere. Nature 319, 305–308.

Ferus, M., Pietrucci, F., Saitta, A.M., Knížek, A., Kubelík, P., Ivanek, O., Shestivska, V., Civiš, S., 2017. Formation of nucleobases in a Miller-Urey reducing atmosphere. Proc. Natl. Acad. Sci. U. S. A. 114, 4306–4311.

Furukawa, Y., Nakazawa, H., Sekine, T., Kobayashi, T., Kakegawa, T., 2015. Nucleobase and amino acid formation through impacts of meteorites on the early ocean. Earth Planet. Sci. Lett. 429, 216–222.

Furukawa, Y., Sekine, T., Oba, M., Kakegawa, T., Nakazawa, H., 2008. Biomolecule formation by oceanic impacts on early earth. Nat. Geosci. 2, 62–66.

Gerasimov, M.V., Ivanov, B.A., Yakovlev, O.I., Dikov, Y.P., 1999. Physics and chemistry of impacts, in: Laboratory Astrophysics and Space Research. Springer Netherlands, Dordrecht, pp. 279–329.

Goldman, N., Reed, E.J., Fried, L.E., William Kuo, I.F., Maiti, A., 2010. Synthesis of glycine-containing complexes in impacts of comets on early earth. Nat. Chem. 2, 949–954.

Goldman, N., Tamblyn, I., 2013. Prebiotic chemistry within a simple impacting icy mixture. J. Phys. Chem. A 117, 5124–5131.

Ishimaru, R., Senshu, H., Sugita, S., Matsui, T., 2010. A hydrocode calculation coupled with reaction kinetics of carbon compounds within an impact vapor plume and its implications for cometary impacts on galilean satellites. Icarus 210, 411–423.

Kitadai, N., Maruyama, S., 2018. Origins of building blocks of life: A review. Geoscience Frontiers 9, 1117–1153.

Lowe, D.R., Byerly, G.R., 2018. The terrestrial record of late heavy bombardment. New Astron. Rev. 81, 39–61.

Magrino, T., Pietrucci, F., Saitta, A.M., 2021. Step by step strecker amino acid synthesis from ab initio prebiotic chemistry. J. Phys. Chem. Lett. 12, 2630–2637.

Marchi, S., Bottke, W.F., Cohen, B.A., Wünnemann, K., Kring, D.A., McSween, H.Y., De Sanctis, M.C., O'Brien, D.P., Schenk, P., Raymond, C.A., Russell, C.T., 2013. High-velocity collisions from the lunar cataclysm recorded in asteroidal meteorites. Nat. Geosci. 6, 303–307.

Martins, Z., Price, M.C., Goldman, N., Sephton, M.A., Burchell, M.J., 2013. Shock synthesis of amino acids from impacting cometary and icy planet surface analogues. Nat. Geosci. 6, 1045–1049.

McKay, C.P., Borucki, W.J., 1997. Organic synthesis in experimental impact shocks. Science 276, 390–392.

Michaelides, A., Liu, Z.P., Zhang, C.J., Alavi, A., King, D.A., Hu, P., 2003. Identification of general linear relationships between activation energies and enthalpy changes for dissociation reactions at surfaces. Journal of the American Chemical Society 125, 3704–3705. URL: https://doi.org/10.1021/ja027366r, doi:10.1021/ja027366r, arXiv:https://doi.org/10.1021/ja027366r. pMID: 12656593.

Mukhin, L.M., Gerasimov, M.V., Safonova, E.N., 1989. Origin of precursors of organic molecules during evaporation of meteorites and mafic terrestrial rocks. Nature 340, 46–48.

Ochiai, Y., Ida, S., Shoji, D., 2024. Monte carlo simulation of UV-driven synthesis of complex organic molecules on icy grain surfaces. Astron. Astrophys. 687, A232.

Pierazzo, E., Kring, D.A., Melosh, H.J., 1998. Hydrocode simulation of the chicxulub impact event and the production of climatically active gases. J. Geophys. Res. 103, 28607–28625.

Roy, D., Najafian, K., von Ragué Schleyer, P., 2007. Chemical evolution: the mechanism of the formation of adenine under prebiotic conditions. Proc. Natl. Acad. Sci. U. S. A. 104, 17272–17277.

Saladino, R., Crestini, C., Costanzo, G., Negri, R., Di Mauro, E., 2001. A possible prebiotic synthesis of purine, adenine, cytosine, and 4(3h)-pyrimidinone from formamide: implications for the origin of life. Bioorg. Med. Chem. 9, 1249–1253.

Salamone, M., Galeotti, M., Romero-Montalvo, E., van Santen, J.A., Groff, B.D., Mayer, J.M., DiLabio, G.A., Bietti, M., 2021. Bimodal Evans–Polanyi relationships in hydrogen atom transfer from C(sp3)–h bonds to the cumyloxyl radical. a combined time-resolved kinetic and computational study. J. Am. Chem. Soc. 143, 11759–11776.

Sanderson, R., 1976. Chemical bonds and bonds energy. volume 21. Elsevier.

Schaefer, L., Fegley, Jr, B., 2010. Chemistry of atmospheres formed during accretion of the earth and other terrestrial planets. Icarus 208, 438–448.

Sekine, T., Kobayashi, T., Nishio, M., Takahashi, E., 2008. Shock equation of state of basalt. Earth Planets Space 60, 999–1003.

Sekine, Y., Sugita, S., Shido, T., Yamamoto, T., Iwasawa, Y., Kadono, T., Matsui, T., 2005. The role of Fischer–Tropsch catalysis in the origin of methane-rich titan. Icarus 178, 154–164.

Shimamura, K., Shimojo, F., Nakano, A., Tanaka, S., 2016. Meteorite impact-induced rapid NH3 production on early earth: Ab initio molecular dynamics simulation. Sci. Rep. 6, 38953.

Shimamura, K., Shimojo, F., Nakano, A., Tanaka, S., 2019. Ab initio molecular dynamics study of prebiotic production processes of organic compounds at meteorite impacts on ocean. J. Comput. Chem. 40, 349–359.

Sugita, S., Schultz, P.H., 2003a. Interactions between impact-induced vapor clouds and the ambient atmosphere: 1. spectroscopic observations using diatomic molecular emission. J. Geophys. Res. 108.

Sugita, S., Schultz, P.H., 2003b. Interactions between impact-induced vapor clouds and the ambient atmosphere: 2. theoretical modeling. J. Geophys. Res. 108.

Sutton, J.E., Vlachos, D.G., 2012. A theoretical and computational analysis of linear free energy relations for the estimation of activation energies. ACS Catalysis 2, 1624–1634. URL: https://doi.org/10.1021/cs3003269, doi:10.1021/cs3003269, arXiv:https://doi.org/10.1021/cs3003269.

Takehara, H., Shoji, D., Ida, S., 2022. Monte carlo simulation of sugar synthesis on icy dust particles intermittently irradiated by UV in a protoplanetary disk. Astron. Astrophys. Suppl. Ser. 662, A76.

Takeuchi, Y., Furukawa, Y., Kobayashi, T., Sekine, T., Terada, N., Kakegawa, T., 2020. Impact-induced amino acid formation on hadean earth and noachian mars. Sci. Rep. 10, 9220.

Wang, S., Temel, B., Shen, J., Jones, G., Grabow, L.C., Studt, F., Bligaard, T., Abild-Pedersen, F., Christensen, C.H., Norskov, J.K., 2011. Universal bronsted-evans-polanyi relations for c–c, c–o, c–n, n–o, n–n, and o–o dissociation reactions. Catalysis Letters 141, 370–373. URL: https://doi.org/10.1007/s10562-010-0477-y, doi:10.1007/s10562-010-0477-y.

Yang, T.T., Saidi, W.A., 2024. The bell-evans-polanyi relation for hydrogen evolution reaction from first-principles. npj Computational Materials 10, 1–6.

Appendix A. Estimation of the model parameters α and β

Here, we consider the reaction $A \underset{2}{\overset{1}{\rightleftharpoons}} B$. If we assume that the linear relationship $\Delta^{\ddagger}G° = \alpha\Delta_r G° + \beta$ applies to each reaction, the standard Gibbs energies of activation for the forward reaction (1) and the reverse reaction (2) can be expressed as follows.

$$\Delta^{\ddagger}G_1° = \alpha_1 \Delta_r G_1° + \beta_1, \tag{24}$$

$$\Delta^{\ddagger}G_2° = \alpha_2 \Delta_r G_2° + \beta_2. \tag{25}$$

When the reaction rate constants are described by the Eyring equation (Eq. (3)), the ratio of the rate constants k_1 and k_2 can be expressed as:

$$\frac{k_1}{k_2} = \frac{\frac{\kappa k_B T}{h}\exp\left(-\frac{\Delta^{\ddagger}G_1°}{RT}\right)}{\frac{\kappa k_B T}{h}\exp\left(-\frac{\Delta^{\ddagger}G_2°}{RT}\right)} = \exp\left(-\frac{(\alpha_1 + \alpha_2)\Delta_r G_1° + (\beta_1 - \beta_2)}{RT}\right), \tag{26}$$

where $\Delta_r G_1^\circ$ is the standard reaction Gibbs energy for the reaction A $\longrightarrow$ B. This derivation employs the relationships $\Delta_r G_2^\circ = -\Delta_r G_1^\circ$ and $\Delta_r G^\circ = \Delta^\ddagger G_1^\circ - \Delta^\ddagger G_2^\circ$. Based on equilibrium theory and kinetics, this ratio k_1/k_2 is equal to $\exp\left(-\frac{\Delta_r G_1^\circ}{RT}\right)$. By comparing these expressions, the following conditions for α and β are obtained:

$$\alpha_1 + \alpha_2 = 1, \tag{27}$$

$$\beta_1 - \beta_2 = 0. \tag{28}$$

In this study, we assume the simplest case, where $\alpha_1 = \alpha_2 = 0.5$. While the above equation does not constrain the value of β, we adopt a range of $\beta = 250 - 350$ kJ/mol, based on comparisons between our calculations and the results of Ishimaru et al. (2010). Additionally, we assume that the values of α and β remain constant across all reactions for simplicity.

Appendix B. Derivation of a time step in the chemical reaction calculation

In our model, at each reaction step, multiple candidates for the next reaction are enumerated. The set of these candidate reactions varies not only between simulations but also between individual trials or steps, even within the same simulation. This leads to the possibility that, in one step, all candidate reactions have high reaction rates, while in another step, all candidates exhibit low reaction rates. Consequently, the time steps corresponding to these steps differ significantly. For instance, in a system where reaction rates are generally high, such as at high temperatures, the time step for a single reaction step is expected to be much shorter than in a system where reaction rates are low, such as at low temperatures. However, time step evaluation was not conducted in the previous study by Ochiai et al. (2024), as their focus was on systems with constant temperature and where reaction rates did not vary significantly from step to step due to the predominance of barrierless reactions. In this study, we quantitatively evaluate the time step associated with each reaction step by comparing it with the kinetic model scheme.

In kinetic models, the change in concentration of chemical species J in one time step Δt, $\Delta[J]$, is written as:

$$\Delta[J] = (r_{J+} - r_{J-})\Delta t, \tag{29}$$

where r_{J+} and r_{J-} are rates of the reactions that produce and consume J, respectively.

In our Monte Carlo calculation, the change in concentration of chemical species J in the reaction step i of a given reaction sequence (hereafter, subscript i means the value at the i-th step) is written as:

$$\Delta[J]_i = \frac{(r_{J+,i} - r_{J-,i})}{\sum r_i}\Delta c_i \tag{30}$$

where $\sum r_i$ represents the sum of reaction rates of the reaction candidates. Δc_i is the concentration change during a single reaction step (the i-th step in this case) and is written as:

$$\Delta c_i = C_i|\Delta M|, \tag{31}$$

where C_i is the concentration corresponding to a single molecule in the molecular set in our simulation, and ΔM is the change in the number of molecules in the molecular set during a reaction step. Using the concentration of the system being simulated (in this study, the impact vapor plume) P_i/RT_i and the total number of molecules in the molecular set $N_{\mathrm{molecules,i}}$, C_i is calculated as:

$$C_i = \frac{P_i/RT_i}{N_{\mathrm{molecules,i}}}. \tag{32}$$

In this model, ΔM is restricted to ± 1 or ± 2 as illustrated in Fig. 1. For simplicity, when considering the case where $\Delta M \pm 1$, Δc_i is directly derived as C_i from Eq. (31). From Eqs. (29) and (30), Δt_i, the time step of the i-th step, is obtained as follows:

$$\Delta t_i = \frac{\Delta c_i}{\sum r_i} = \frac{\Delta c_i}{\sum \left(k_{\mathrm{first,i}}C_i + k_{\mathrm{second,i}}C_i^2\right)} = \frac{1}{\sum k_{\mathrm{first,i}} + C_i \sum k_{\mathrm{second,i}}} \; \mathrm{s}. \tag{33}$$

where $k_{\mathrm{first,i}}$ and $k_{\mathrm{second,i}}$ are the rate constants of first-order reactions and second-order reactions, respectively. Thus, Δt_i is regulated by the reaction rates of the reaction candidates at that step and is dominated by the fastest reaction among the candidates.